Modeling the observed proton aurora and ionospheric convection responses to changes in the IMF clock angle: 2. Persistence of ionospheric convection

Article

Published Version

CentAUR

Central Archive at the University of Reading

Reading's research outputs online

Modeling the observed proton aurora and ionospheric convection responses to changes in the IMF clock angle:
2. Persistence of ionospheric convection

M. Lockwood,[1,2] B. S. Lanchester,[1] S. K. Morley,[1] K. Throp,[1] S. E. Milan,[3] M. Lester,[3] and H. U. Frey[4]

[1] We apply a numerical model of time-dependent ionospheric convection to two directly driven reconnection pulses during a 15-min interval of southward IMF on 26 November 2000. The model requires an input magnetopause reconnection rate variation, which is here derived from the observed variation in the upstream IMF clock angle, θ. The reconnection rate is mapped to an ionospheric merging gap, the MLT extent of which is inferred from the Doppler-shifted Lyman-α emission on newly opened field lines, as observed by the FUV instrument on the IMAGE spacecraft. The model is used to reproduce a variety of features observed during this event: SuperDARN observations of the ionospheric convection pattern and transpolar voltage; FUV observations of the growth of patches of newly opened flux; FUV and in situ observations of the location of the Open-Closed field line Boundary (OCB) and a cusp ion step. We adopt a clock angle dependence of the magnetopause reconnection electric field, mapped to the ionosphere, of the form $E_{no}\sin^4(\theta/2)$ and estimate the peak value, E_{no}, by matching observed and modeled variations of both the latitude, Λ_{OCB}, of the dayside OCB (as inferred from the equatorward edge of cusp proton emissions seen by FUV) and the transpolar voltage Φ_{PC} (as derived using the mapped potential technique from SuperDARN HF radar data). This analysis also yields the time constant τ_{OCB} with which the open-closed boundary relaxes back toward its equilibrium configuration. For the case studied here, we find $\tau_{OCB} = 9.7 \pm 1.3$ min, consistent with previous inferences from the observed response of ionospheric flow to southward turnings of the IMF. The analysis confirms quantitatively the concepts of ionospheric flow excitation on which the model is based and explains some otherwise anomalous features of the cusp precipitation morphology.

1. Introduction

[2] In a companion paper, *Throp et al.* [2005, hereafter referred to as Paper I] we analyze the time constants for the decay of the proton aurora following two brief pulses of magnetopause reconnection. In the present paper, we discuss the corresponding relaxation time constants for ionospheric convection and the latitude of the dayside open-closed field line boundary. Paper I also presented

some modeled results on the spatial pattern of proton aurora emissions for this event, and we here give the details of the derivation of the convection patterns used to make these predictions. Both studies are based on the event on the 26 November 2000 reported by *Lockwood et al.* [2003, hereafter referred to as LEA03] in which a double brightening of Lyman-α emission in the dayside cusp was observed by the SI-12 channel of the FUV instrument on the IMAGE satellite [*Mende et al.*, 2000a, 2000b]. These two brightenings occurred in response to two short-lived swings of the Interplanetary Magnetic Field (IMF) toward a southward orientation, during a period of strongly enhanced solar wind plasma concentration. Figures 1b and 1c of Paper I summarize the solar wind and interplanetary conditions prevailing during this event.

[3] We here employ the numerical model of *Lockwood and Morley* [2004, hereafter LM04], to predict the evolution of ionospheric convection flows to simulate the variations in transpolar voltage. This is done using a novel application of

[1]Department of Physics and Astronomy, Southampton University, Southampton, Hampshire, UK.
[2]Also at Rutherford Appleton Laboratory, Chilton, Oxfordshire, UK.
[3]Department of Physics and Astronomy, Leicester University, Leicester, UK.
[4]Space Sciences Laboratory, University of California, Berkeley, Berkeley, California, USA.

the LM04 model in which the magnetopause reconnection rate, ε, is an input to the model. As well as predicting the convection, the model calculates the variations in the latitude Λ_{OCB} of the dayside OCB. The predicted variations are then compared with observations by the SuperDARN radar network and the IMAGE satellite. The transpolar voltage Φ_{PC}, calculated from SuperDARN line-of-sight velocity data using the method of *Ruohoniemi and Baker* [1998], is shown in Figure 1d of Paper I. Because radar echoes are scarce or absent in several regions, we here check the derived potential differences using flow data from DMSP (Defense Meterological Satellite Program) satellites. The latitude of the equatorward edge of cusp precipitation (close to the OCB) is shown in Figure 1e of Paper I, as derived from the OI "electron" emission observed by the SI-13 channel of FUV. This latitude has also been estimated using the equatorward edge of the cusp proton aurora observed by FUV/SI-12. Both these estimates agree very well with the OCB location inferred from particle observations during overpasses of DMSP spacecraft [LEA03].

[4] Magnetopause reconnection during southward IMF converts closed flux into open flux. In general, this has two competing effects in the ionosphere: (1) the OCB can migrate equatorward in the Earth's frame and (2) poleward flow in the Earth's frame can be excited. Quantitatively, the flow across the OCB in its own rest frame is given by $V' = (E_n/B_i) = V_c - V_b$, where E_n is the tangential electric field along the OCB in the boundary rest frame, B_i is the ionospheric field strength and V_c and V_b are the poleward velocities, normal to the OCB in the Earth's frame of reference, of the plasma flow and the boundary motion, respectively.

[5] If no equatorward erosion of the OCB occurs where reconnection is ongoing ($V_b = 0$, $V_c = V' > 0$), then V_c is proportional to E_n. Thus convection, and associated field-aligned currents, increase in synchronization with the reconnection electric field, E_n, as envisaged by *Banks et al.* [1984] and *Clauer and Banks* [1986]. In the Cowley-Lockwood model, on the other hand, a rise in E_n (and hence V') causes both a rise in V_c and increasingly negative V_b. While $V_b < 0$, V_c is reduced for a given V'. However, on longer timescales there is no net migration of the OCB and so the average V_b tends to zero and the average V_c approaches the average V'. Thus the equatorward erosion of the OCB causes a smoothed and delayed flows response to pulses in E_n. Because this smoothing and delay requires changes in the magnetic field between the magnetopause and the ionosphere, as given by Faraday's induction law [*Lockwood and Cowley*, 1992], we here refer to this as "inductive smoothing." Observations of smoothed convection responses and of initial OCB erosion (at a rate $V_b = -a(d\Lambda_{OCB}/dt)$, where one degree of invariant latitude corresponds to a meridional distance a) are therefore qualitatively consistent with the theory of *Cowley and Lockwood* [1992].

[6] The equatorward erosion of the dayside OCB following magnetopause reconnection is well documented in the literature. It is observed in statistical surveys of the equatorward latitude of cusp precipitation [*Burch*, 1973; *Newell and Meng*, 1992; *Stubbs et al.*, 2001], as well as in time-series data on the equatorward edge of the 630 nm (oxygen "red-line") cusp aurora [*Eather*, 1985; *Horwitz*

and Akasofu, 1977; *Sandholt et al.*, 1985; *Sandholt*, 1988; *Vorobjev et al.*, 1975; *Leontyev et al.*, 1992]. In addition, the effect has been observed in radar observations of flows and ionospheric gradients associated with the OCB [*Freeman and Southwood*, 1988; *Lockwood et al.*, 1993; *McCrea et al.*, 2000; *Milan et al.*, 2003; *Moen et al.*, 2004; *Lockwood et al.*, 2005].

[7] In addition, the transpolar voltage is observed to rise following southward turnings of the IMF. This effect was also first noted in statistical surveys of satellite data [e.g., *Reiff et al.*, 1981; *Wygant et al.*, 1983] and then in time series data from inversion of observations from global networks of magnetometers [*Lu et al.*, 1989, 2002; *Ahn et al.*, 1992; *Knipp et al.*, 1991, 1993; *Ridley et al.*, 1997, 1998]. These inversions have generally employed the AMIE (Assimilative Mapping of Ionospheric Electrodynamics) technique. The effect has also been observed in data from the SuperDARN network of HF radars [*Ruohoniemi and Greenwald*, 1998; *Ruohoniemi et al.*, 2002; LEA03].

[8] Thus equatorward erosion of the cusp and an increase in the transpolar voltage are two known consequences of a rise in the magnetopause reconnection voltage caused by a swing of the IMF to a more southward orientation. In this paper, we look at the time constants for these effects using the LM04 model and show quantitatively that they are interrelated in the manner predicted by the Cowley-Lockwood theory of ionospheric flow excitation.

2. Large-Scale Convection Model

[9] The *Cowley and Lockwood* [1992] theory of iono-spheric convection excitation predicts that the onset of the response to a change in IMF B_z component follows immediately after the arrival of the consequent Alfvén wave in the ionosphere. On the other hand, the full change in ionospheric flows will be suppressed for a time which allows for the dayside magnetosphere-ionosphere system to come to equilibrium with the new amount of open flux. The LM04 numerical model implements this theory to reproduce the effects of general variations of reconnection rate in space and time. We here specify the dayside reconnection rate input to the LM04 model from the observed IMF clock angle θ using the empirical relation:

$$E_n(MLT, t_s) = E_{no} \sin^4 \{\theta(t_s - \Delta t)/2\}. \quad (1)$$

[10] E_n is the electric field tangential to the dayside ionospheric merging gap at a given MLT and simulation time t_s. It is therefore the ionospheric projection of the magnetopause reconnection rate. For purely southward IMF (θ = π) E_n equals its peak value, E_{no}. The dependence on clock angle in equation (1) has been found in optimum solar wind-magnetosphere coupling functions from studies of geomagnetic activity [*Akasofu*, 1981; *Vasyliunas et al.*, 1982; I. Finch, private communication, 2005] and has been reproduced by simulations of magnetopause reconnection voltage in global MHD models [*Fedder et al.*, 1991]. E_n is computed from the IMF clock angle observed a time ($t_s - \Delta t$), where Δt is the propagation lag from the IMF monitor to the ionospheric merging gap at the MLT in question. At the nose of the magnetosphere, Δt is equal to the lag δt discussed in Paper I; however, in general, Δt exceeds δt
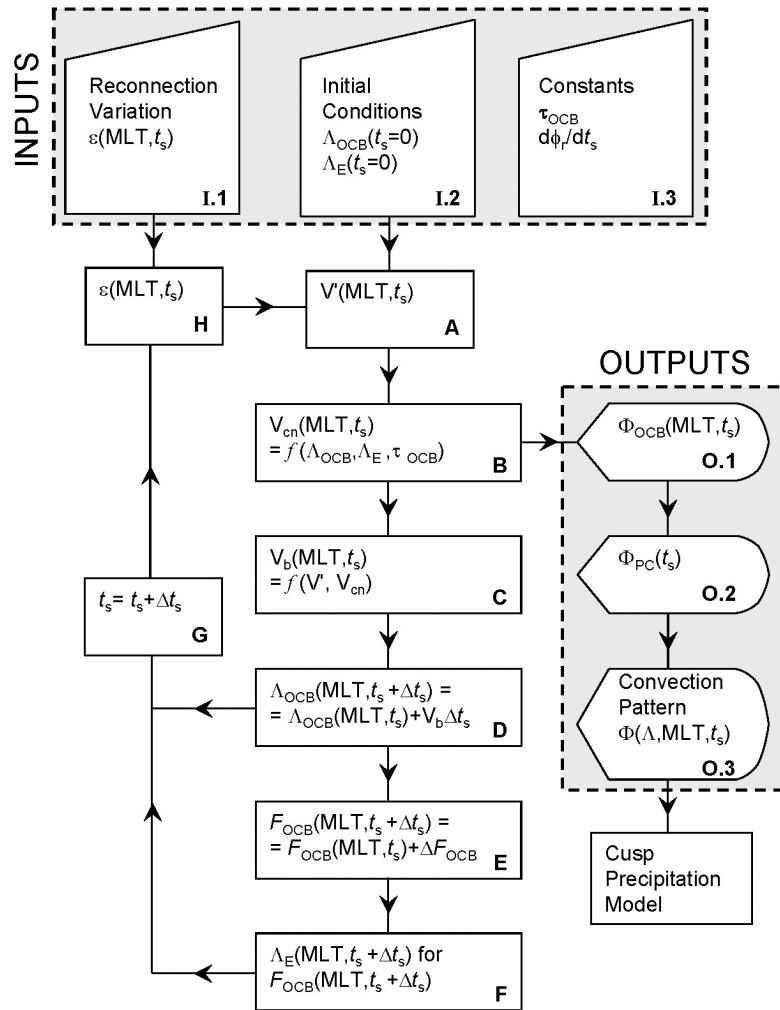
Figure 1. Flowchart of the LM04 model of time-dependent ionospheric convection, defining the inputs, operations, and outputs. Input I.1 is the reconnection rate variation ε which is derived from the observed IMF orientation variation and is a function of MLT and simulation time t_s. Input I.2 is the initial positions of the OCB latitude and its equilibrium position (Λ_{OCB} and Λ_E) and input I.3 is two constants, the time constant τ_{OCB} (see text for details) and the rate of longitudinal expansion of changes in ε, $d\phi_r/dt$. In operation A, the ionospheric velocity across the OCB in its own rest frame, V', is computed from ε and in step B the convection velocity V_c with which the OCB will return toward its equilibrium location is computed from the displacement of Λ_{OCB} from Λ_E and the time constant for that return, τ_{OCB}. This yields the boundary velocity $V_b = V_c - V'$ (step C). In step D, the new boundary latitude $\Lambda_{OCB}(MLT, t_s + \Delta t_s)$ is computed for the next simulation time (Δt_s later) from V_b, and in step E the new equilibrium boundary latitude, for the updated amount of newly opened flux $\Lambda_E(MLT, t_s + \Delta t_s)$, is calculated. All these parameters are functions of MLT and simulation time t_s. The model then advances the time by Δt_s (step G) and finds the new reconnection rate from input I.1 (step H). From the convection velocity perpendicular to the OCB, the electric field and electrostatic potential Φ_{OCB} along the OCB is known and is tapped off after step B to give output O.1. The peak difference in Φ_{OCB} is the transpolar voltage Φ_{PC} (output O.2) and solutions of Laplace's equation for the auroral zone and polar cap separately yield the pattern of ionospheric flow equipotentials (output O.3).

away from noon as the reconnection propagates over the magnetopause. The initial conditions for the simulation ($t_s = 0$) are a circular polar cap containing open flux of $F_{PC}(t_s = 0)$. The open flux at a later time t_s is given by adding to $F_{PC}(t_s = 0)$ the integrated difference between the magnetopause and tail reconnection voltages over the interval between time zero and t_s, $\Delta F_{pc}(t_s)$. As the newly opened

flux ΔF_{pc} is added to the system, the OCB erodes equatorward at the footprint of the magnetopause X-line. This perturbation propagates tailward. In the theory of Cowley and Lockwood, the polar cap expands toward a new equilibrium position at lower latitudes at all local times. This evolution represents the response of the boundaries to newly opened flux being transported into the tail lobes
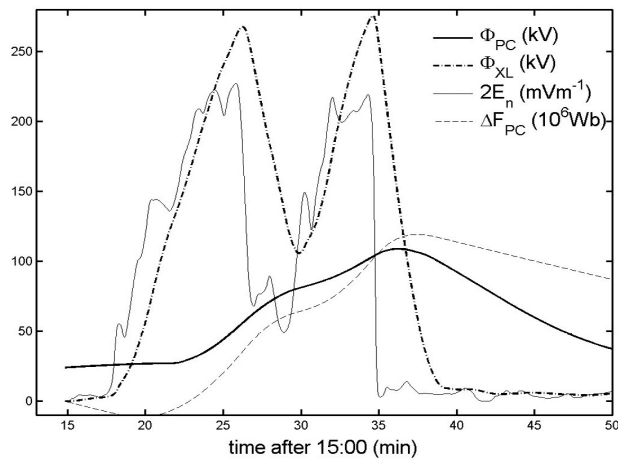
Figure 2. Inputs to and outputs from the LM04 model of ionospheric convection applied to 26 November 2000. E_n (solid line) is the electric field at noon tangential to the ionospheric OCB, in its own rest frame (proportional to the magnetopause reconnection rate), specified by the lagged IMF clock angle observed by ACE. (Note that $2E_n$ has been plotted to best exploit the common y-axis scale of the plot). The integrated voltage along the entire X-line at any one instant, Φ_{XL}, is shown by the dot-dash line. The thin dashed line gives ΔF_{PC}, the difference in F_{PC} with respect to the initial value $F_{PC}(t_s = 0)$. The transpolar voltage generated by the model, Φ_{PC}, is shown by the thick solid line.

through the action of the solar wind [LM04]. At each simulation time step ($\delta t_s = 1s$) the spatial distribution of the reconnection rate is updated as are the OCB and equilibrium boundary locations. From the velocity with which the OCB is tending back toward the equilibrium latitude, along with the distribution of E_n around the OCB at that time, the distribution of potential around the OCB is obtained; from this the transpolar voltage is derived and solving Laplace's equation (by assuming a uniform spatial distribution of ionospheric conductivity) yields the convection pattern. The final two panels in Figure 2 of Paper 1 show that a substorm expansion commences at about 1546 and thus the interval of southward IMF represents the growth phase of this substorm. We assume that before this substorm onset the tail reconnection voltage is constant. The model is run here with a reconnection voltage of 20 kV along a fixed X-line in the cross-tail current sheet to match the observed transpolar voltage and the observed poleward retreat of the dayside OCB when the IMF clock angle θ fell below 50°.

[11] Note that the LM04 model employed here is similar in concept, and in many details, to that presented by *Freeman* [2003]. However, one important difference for our application is that the Freeman model assumes that both the OCB and the equilibrium boundary remain circular in form at any one time, whereas the LM04 model allows more localized dayside erosions to form by considering the latitude of both these boundaries to be a function of MLT.

[12] Figure 1 summarizes the LM04 model with a flowchart, giving the inputs, outputs, and operations. The variations of the inputs to, and some of the outputs from, the model applied to the event on 26 November 2000 are

shown in Figure 2. The thin line gives the electric field along the ionospheric merging gap at noon, $E_n(MLT = 12, t_s)$. This is the magnetopause reconnection rate mapped down field lines to the noon merging gap, computed from the IMF clock angle θ, as observed by ACE, using equation (1). In Figure 2, E_{no} is set to 114 mV m^{-1}: the effect of varying E_{no} will be studied later in this paper. The delay δt (Δt for noon) is as derived, to within an uncertainty of ±2.2 min, by Figure 7 of Paper I. The reconnection rate changes in the model propagate away from noon and we here use the same propagation speed as LM04, namely, Δt increases by 1 min per 1 hour of MLT away from noon (thus $d\phi_r/dt = 0.25° \, s^{-1}$). This propagation continues to the ends of the merging gap at MLTs of 0900 and 1500, on the dawn and dusk flanks, respectively. These MLTs are the minimum and maximum MLT over which the proton aurora images show newly opened field lines during this event (see Figure 2 of Paper I or Figure 4 of LEA03). This assumes that the solar wind concentration is high enough to reveal all newly opened flux in the FUV/SI-12 images, even if it is produced on the magnetopause flanks where sheath concentrations are lower than at noon as in the simulations shown in Figure 9 of Paper I. The dot-dash line in Figure 2 shows the variation in the total merging gap voltage Φ_{XL} obtained by integrating E_n along the merging gap at any one time. The thin dashed line in Figure 2 shows the change in the polar cap flux, ΔF_{PC}. When Φ_{XL} is small, the decline in ΔF_{PC} reveals the effect of the tail voltage of 20 kV, and when Φ_{XL} exceeds this level, ΔF_{PC} increases as the rate of production of open flux outstrips the rate at which it is lost. Last, the thick solid line shows the variation of the transpolar voltage Φ_{PC} generated by the model. Note that the Φ_{PC} variation is effectively the input Φ_{XL} variation which has been inductively smoothed. The parameter which controls this smoothing in the model is the OCB relaxation time constant τ_{OCB} (LM04), which has here been set to 10 min, as in the simulations by LEA03. Later in this paper, we will discuss the effect of changing τ_{OCB}.

[13] In order to compare model results with observations made on 26 November 2000, initial conditions need to be matched to those prevailing on this day. As the latitude of the OCB, Λ_{OCB}, determines the amount of open flux present in the polar cap, the initial polar cap flux $F_{PC}(t_s = 0)$ is set to match observations of Λ_{OCB} made by the IMAGE FUV instrument (Input I.2). Figure 3 shows how a circular OCB can be fitted to the highest intensity dayside Doppler-shifted Lyman-α emissions (using a threshold high enough to remove background emissions) seen by FUV/SI-12 at 1522 UT. The thick solid line places the northward-IMF cusp "spot" on open field lines and the main proton aurora at all other local times on closed field lines. Also shown in Figure 3 (as thick black lines) are segments of DMSP passes where the ion and electron precipitations observed are consistent with open field lines. These passes all took place during for the interval 1436–1520 prior to the swings to southward IMF. Close to midnight, the poleward edge of the proton aurora detected is considerably equatorward of this circular boundary. This could be interpreted as showing that the open polar cap was not circular. Alternatively, there may have been subvisual closed field lines in this region, as has often been inferred for quiet intervals and substorm growth phases [*Elphinstone et al.*, 1991, 1992; *Samson et al.*,

1992]. If this region contains open, rather than the subvisual closed flux inherent in the circular OCB adopted, then the main effect on the analysis presented here is that open flux estimates are consistently too small. The image taken 8 min later (see Figure 9) reveals some weak nightside Lyman-α emission within much of this region and even within the inferred OCB location, implying that on the nightside the true OCB latitude may be greater than shown in Figure 3, making the true open flux smaller rather than larger. This highlights the great sensitivity of any open flux estimate to the intensity threshold adopted in attempting to define the OCB. For this reason we do not here attempt to define the variation in the open flux F_{PC}. Rather, we model the change in open flux ΔF_{PC} (see Figure 2) and compare it to the amount of newly opened flux that is revealed on the dayside in the FUV/SI-12 images. The OCB estimate in Figure 3 has a radius of $16°$ and has a center that is offset from the magnetic pole toward the nightside by $0.7°$ and toward dawn by $1.2°$. This sets a nominal initial polar cap flux $F_{PC}(t_s = 0)$ of 6.1×10^8 Wb, and places the noon OCB at a latitude of $74.7°$. In the initial conditions the ionosphere-magnetosphere system is assumed to have reached an equilibrium and so $\Lambda_{OCB}(t_s = 0) = \Lambda_E(t_s = 0)$ at all MLT.

[14]   To summarize the inputs to the model: $F_{OCB}(t_s = 0)$ is set at 6.1×10^8 Wb, where $t_s = 0$ corresponds to 1515 UT; E_n is set by the observed (lagged) IMF clock angle using equation (1) with a value of E_{no} which we initially set at 114 kV, but which we will later match to the observations; a constant reconnection voltage of 20 kV closing open field lines in the cross-tail current sheet is applied (between 2100 and 0300 MLT); the maximum extent of the dayside ionospheric merging gap is set at 0900−1500 MLT to match the observed maximum extent of cusp proton aurora.

[15]   Note that solution of Laplace's equation is carried out for the polar cap and for the auroral oval separately and it is assumed that ionospheric conductivity in those regions is uniform. Thus although a conductivity difference between the polar cap and the auroral oval is allowed for, variations in those conductivities within the two regions is not. Such structure would be associated with spatial precipitation structure and with the daylight terminator. Analytic solution of Laplace's equation for such conductivity structure, even if it could be characterized, would be very complex and is not included in the model. In this paper, we are mainly concerned with the total flux transport rate across the polar cap, the transpolar voltage Φ_{PC}, and although conductivity gradients can alter the flow streamlines within the polar cap, they cannot alter Φ_{PC} for a given potential distribution around the polar cap, $\Phi_{OCB}(MLT)$. The only effect of spatial conductivity structure on these voltages is therefore via the time constant τ_{OCB} which we here assume to be constant but is varied to fit the observations.

[16]   Thus the one key parameter in the LM04 model, and one which controls the degree of inductive smoothing of the flows, is the time constant τ_{OCB} with which the OCB
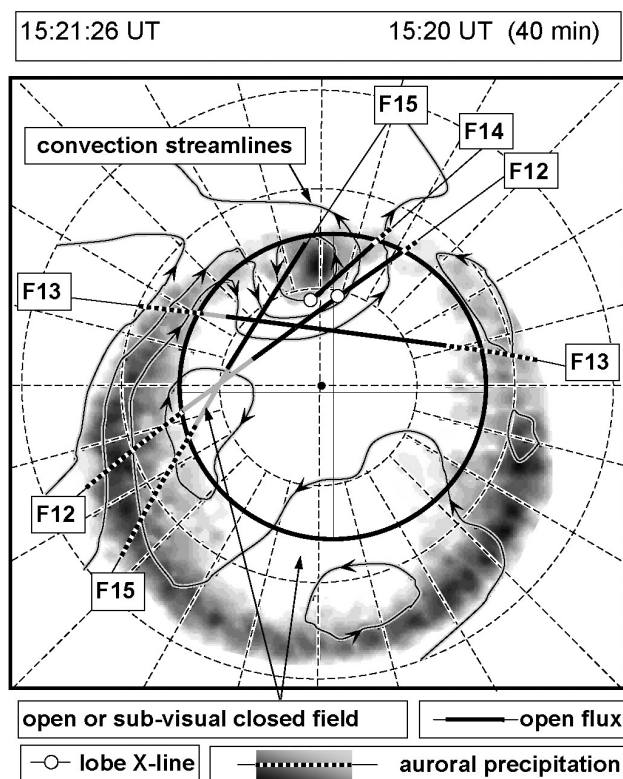
Figure 3. Image of the Doppler-shifted Lyman-α emission seen by the FUV/SI-12 instrument on the IMAGE spacecraft at 15:22 UT on 26 November 2000, with superposed convection flow streamlines derived from the SuperDARN radar scans commencing at 1520. These equipotentials are derived using the "mapped-potential" technique with a predicted ACE-to-ionosphere lag of 40 min. The thick solid line is a circular estimate of the dayside OCB location which places the northward-IMF cusp "spot" and lobe cell sunward flow on open field lines and the main nightside proton aurora on closed field lines. This would imply a region of sub-visual precipitation on closed field lines in the midnight sector (2200−0300 MLT). The OCB circle shown has a radius of $16°$ and is offset from the magnetic pole toward the nightside by $0.7°$ of invariant latitude and toward dawn by $1.2°$. This sets the initial polar cap flux $F_{PC}(t_s = 0)$ of 6.1×10^8 Wb, and places the noon OCB at a latitude $\Lambda_{OCB}(t_s = 0)$ of $74.7°$. Across this invariant latitude-MLT map of the polar cap are traced northern hemisphere passes by DMSP satellites F12, F14, and F15 and a southern hemisphere pass by F13: because the F13 pass is in the southern hemisphere is has been mapped to the northern hemisphere by mirroring it in MLT about the noon-midnight axis, thereby allowing for dawn-dusk hemispheric asymmetries associated with the IMF B_Y component. The segments of the passes marked by thick black lines are where particle precipitations observed imply open field lines and the black and white dashed segments are where auroral oval precipitation was observed. The segments shaded gray are where the precipitation observed implies either open field lines or subvisual closed field lines. The open circles show observed ionospheric footprints of lobe reconnection sites. These passes were all during the interval before the image was taken and while the IMF was northward. The times of the polar cap traversals (i.e., poleward of the auroral oval) for F12, F13, and F15 are 1439:00−1447:50, 1458:33−1505:00, and 1453:42−1500:42. F14 entered the polar cap during a data gap but left it at 1510:24.
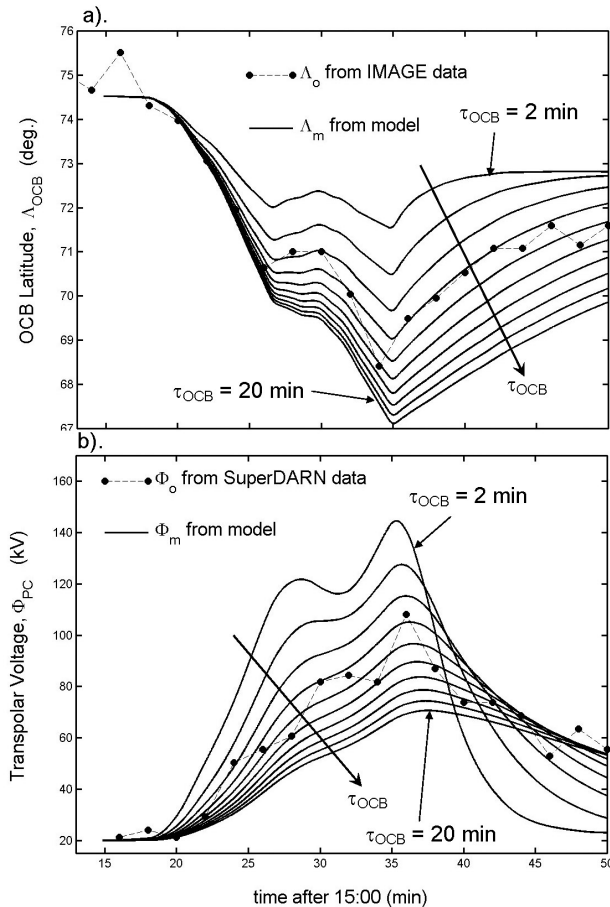
Figure 4. Observed and modeled variations of (a) the latitude of the noon open-closed boundary Λ_{OCB} and (b) the transpolar voltage Φ_{PC}. The dashed lines connecting dots are the observed values (Λ_o and Φ_o) and the solid lines are modeled variations (Λ_m and Φ_m) for various boundary relaxation time constants, τ_{OCB}. Curves are for τ_{OCB} of 2–20 min, in steps of 2 min. The peak electric field employed is $E_{no} = 114$ mV m^{-1}.

relaxes back toward its equilibrium location. In general, this can be a function of MLT but was set to a constant value of 10 min. in LM04: we here consider a range of values between 2 and 20 min. All other inputs to the model are as employed by LM04.

3. Results

### 3.1. Comparison of Modeled and Observed Voltages and Boundary Locations

[17] Figure 4 presents a comparison of the model output with the observations. Figure 4a shows a family of curves of the modeled OCB latitude at noon, Λ_{OCB}, for OCB relaxation time constants τ_{OCB} between 2 and 20 min, in steps of 2 min. The solid points, joined by a dotted line, show the noon OCB latitude inferred from the equatorward edge of proton emissions generated by cusp ion precipitation, as seen by the FUV instrument. These data are scaled from Figure 5a of LEA03, which plots the intensity of oxygen 135.6 nm emission intensity, as seen by SI-13/FUV in the

1200–1230 MLT sector, as a function of latitude and time. LEA03 defined the equatorward edge of the latitudinal band of emission as where the intensity falls to half its peak value (the lower yellow line in their Figure 5a). This equatorward edge of the electron-induced UV emission was found to be a good indicator of the dayside OCB inferred from in situ particle precipitation data (discussed later in Figure 11) from overpasses by various DMSP satellites during this event (see Figures 3 and 10). All curves in Figure 4 are for a fixed peak electric field E_{no} of 114 kV. It can be seen that the model predicts increased erosion when τ_{OCB} is larger and that, for the E_{no} of 114 kV used, the best-fit to the observations is for τ_{OCB} near 10 min.

[18] Figure 4b shows the corresponding model predictions of the transpolar voltage, Φ_{PC}, for the same OCB relaxation time constants τ_{OCB} as used in Figure 4a. It can be seen that when τ_{OCB} is small Φ_{PC} peaks earlier and at larger values and that the variation is more similar in form to the variation of Φ_{XL} as shown in Figure 2. In fact, for $\tau_{OCB} = 0$, Φ_{PC} is the same as Φ_{XL} at all t_s (and the OCB latitude Λ_{OCB} remains constant). Increasing τ_{OCB} causes Φ_{PC} to peak at smaller values than the peak Φ_{XL} and also increases the length of time over which Φ_{PC} is enhanced. Thus increasing τ_{OCB} (and hence from Figure 4a allowing greater erosion) effectively introduces more inductive smoothing of the Φ_{PC} response to Φ_{XL}. The points joined by a dashed line in Figure 4b show the transpolar voltage deduced from the ionospheric flow data from the SuperDARN radar network using the "mapped potential" technique of *Ruohoniemi and Baker* [1998]. The convection streamlines shown in Figure 2 of Paper I are derived by fitting an empirical convection model to the observed line-of-sight velocities made by the Northern Hemisphere SuperDARN network. The model is driven by the (appropriately lagged) upstream IMF conditions. The transpolar voltage is then derived from the fitted potential pattern. It can be seen from Figure 4b that for the E_{no} of 114 kV used, the LM04 model reproduces both the peak height and variation of the SuperDARN Φ_{PC} for a τ_{OCB} of about 10 min.

[19] In several regions radar echoes are scarce or absent and in such regions we have less confidence in the flow streamlines derived by the mapped potential technique (shown as dashed lines in such regions in Figure 2 of Paper 1). To check the potential differences derived from the convection patterns, we here look at the along-track electric field E_x derived from the cross-track plasma velocity V_{CT}, as observed by various DMSP satellites. Integration along the satellite track gives the potential, $\Phi = \int \mathbf{E} \bullet \mathbf{dl} = \int V_{CT} B_i V_s$ dt, where B_i is the magnetic field and V_s is the satellite velocity. One such pass, by the DMSP F12 satellite over the southern polar cap near the peak of the event is discussed later and shown in Figures 10 and 11. (Variations in Φ and V_{CT} during pass are shown in Figure 11). A peak potential difference of 56.6 kV was seen between 1529.9 and 1538.1, when the satellites (invariant latitude, MLT) coordinates were ($-79.8°$, 9.42 hours) and ($-65.4°$, 19.2 hours), respectively. That this voltage is somewhat lower than the average transpolar voltage for this interval, as derived from the SuperDARN data, is not surprising because the satellite does not intersect the centers of the convection cells (see Figure 10). The voltage over this segment of the orbit path in
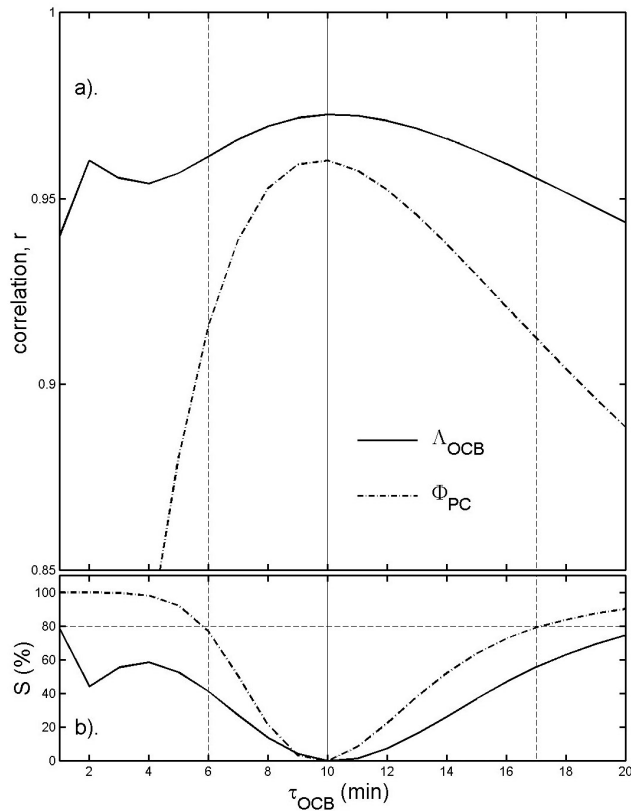
Figure 5. Cross correlation analysis between the observed and modeled variations of the OCB latitude (Λ_o and Λ_m, solid line) and of the transpolar voltage (Φ_o and Φ_m, dot-dash line). (a) The cross correlation coefficients as a function of the model OCB relaxation time constant τ_{OCB}. (b) The significance of the difference between the correlation coefficient and its peak value (found to be for τ_{OCB} = 10 min, marked by the vertical solid line in both panels). The two vertical dashed lines give the τ_{OCB} at which the correlation for the transpolar voltage is lower the peak value, at the 80% significance level (the horizontal dashed line in Figure 5b). At this confidence level the uncertainty range in the best-fit τ_{OCB} is 6−17 min.

the SuperDARN maps for 1530−1539 UT (the duration of the satellite pass through the polar cap) are 54 kV, 48 kV, 42 kV, 66 kV, and 66 kV, giving an average value of 55.2 kV for the duration of the polar cap pass. Thus despite the fluctuation seen during the satellite pass, the average corresponding SuperDARN voltage is very close to that observed by the satellite.

[20] Similarly, the F13 satellite pass shown in Figure 3 gives a good test of the voltage before the onset of the event. The largest voltage observed was 30.6 kV between 1459.7 and 1503.5 UT but this is a vigorous lobe circulation cell, typical of northward IMF conditions which F13 intersected and which is also seen in the SuperDARN flow patterns (e.g., Figure 3). Outside this lobe cell, F12 detected 17.7 kV between 1503.5 UT and 1505.7 UT, when it traveled between (Λ, MLT) of (−77.7°, 15.0 hours) and (−71.4°, 16.5 hours). The SuperDARN data indicate a voltage of 18.8 kV outside of this lobe cell. Thus F13 gives strong support to the SuperDARN voltages before the event

and F12 gives strong support to the larger voltages seen during the event.

3.2. Derivation of the Best-Fit Modeled Convection Patterns

[21] Figure 5 presents a cross-correlation analysis of the observed and modeled variations of Λ_{OCB} and Φ_{PC} as a function of the time constant τ_{OCB}. For each τ_{OCB} the modeled variations of Λ_{OCB} and Φ_{PC}, as shown in Figures 4a and 4b, are cross-correlated with the observed variations for a range of lags between −10 and +10 min. The peak correlation coefficients, as a function of τ_{OCB}, are shown by the solid and the dot-dashed lines in the top panel of Figure 4 for Λ_{OCB} and Φ_{PC}, respectively. Both correlations are strong, peaking at over 0.95 at τ_{OCB} of 10 min. Because all the modeled curves in Figure 4a are similar in form, the correlation coefficient for Λ_{OCB} is not a strong function of τ_{OCB}. On the other hand, Figure 4b shows that the form of the modeled Φ_{PC} varies considerably with τ_{OCB} and hence the dot-dashed line shows a more pronounced peak. The statistical significance of the τ_{OCB} estimates from these peaks is assessed in the lower panel of Figure 5. This shows the significance S of the difference of the correlation coefficient for a given τ_{OCB} and the peak correlation, assessed using the Fisher-Z test [see *Lockwood*, 2002]. The S variations for both Λ_{OCB} and Φ_{PC} (solid and dot-
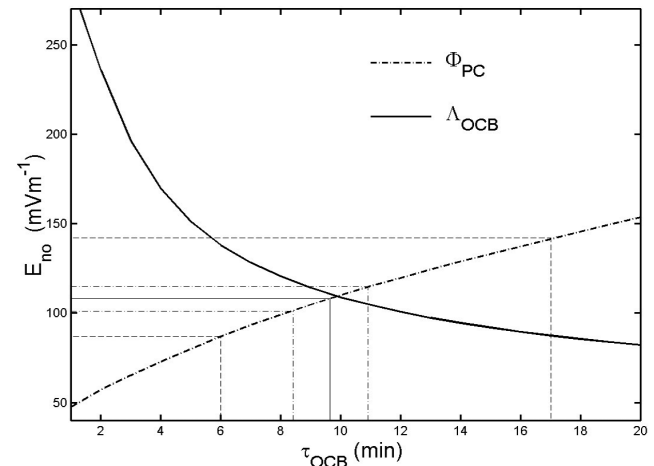
Figure 6. The peak electric field tangential to the OCB, E_{no} (seen when the IMF clock angle θ is equal to π, see equation (1)) needed to give the best-fit correlations shown in Figure 5. The E_{no} to give the best-fit to the observed OCB latitude Λ_{OCB} is the solid curve, the corresponding values for the best fit to the transpolar voltage Φ_{PC} is the dot-dash line. The extreme values of τ_{OCB} from the transpolar voltage correlation study (Figure 5) are marked by vertical dashed lines and from the OCB latitude deviation study (Figure 7) are marked by vertical dot-dashed lines. The best agreement is at τ_{OCB} = 9.7 min. and gives an optimum E_{no} of 108 mV m^{-1} (thin solid lines) and the uncertainty range in τ_{OCB} of 6−17 min derived in Figure 5 gives an uncertainty in E_{no} of 90−143 mVm^{-1} (thin dashed lines). The uncertainty range in τ_{OCB} of 8.4−10.9 min derived in Figure 7 gives an uncertainty in E_{no} of 101−115 mVm^{-1} (thin dot-dash lines).
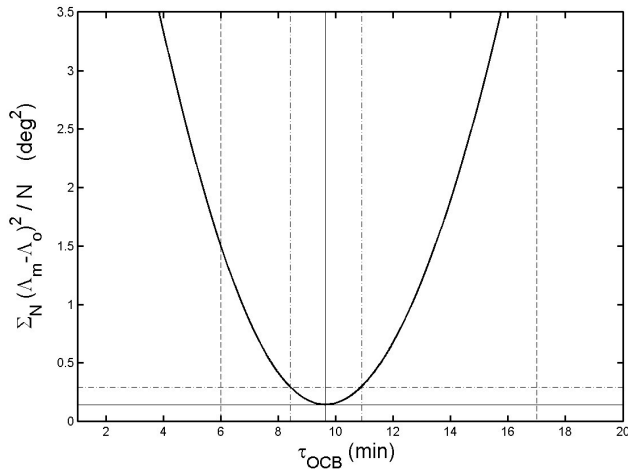
Figure 7. The mean square difference between observed and modeled OCB latitudes (Λ_o and Λ_m, respectively), $\Sigma_N (\Lambda_o - \Lambda_m)^2/N$. The solid line marks the minimum mean-square deviation, Δ_{ms}, which is at τ_{OCB} of 9.7 min. The horizontal dot-dash line is at $(\Delta_{ms} + \delta_{ms})$, where $\delta_{ms} = \delta\Lambda (2/N)^{1/2}$ is the smallest resolvable change in the mean-square difference, where $\delta\Lambda = 0.5°$ is the resolution of each of N measurements of Λ_{OCB}. This sets an uncertainty range in τ_{OCB} of 8.4–10.9 min (marked by vertical dot-dash lines). For comparison, the vertical dashed lines from Figure 5 are also shown.

dashed lines), by definition fall to zero at $\tau_{OCB} = 10$ min where the correlations peak. The horizontal dashed line shows the 80% level for S and it can be seen that for the range of τ_{OCB} used in Figure 5, the correlation for Λ_{OCB} is never significantly different from its peak value (at this 80% confidence level). On the other hand, the correlation for Φ_{PC} is significantly lower than its peak value (at this level) for $\tau_{OCB} < 6$ min and $\tau_{OCB} > 17$ min. Thus although the correlation analysis of Λ_{OCB} does not constrain τ_{OCB}, the corresponding analysis of Φ_{PC} does set an uncertainty range of 6–17 min (using the 80% significance level), with a most likely value of 10 min.

[22] The correlation analysis shown in Figure 5 only compares the shape of the modeled and observed variations, without consideration given to the amplitudes of the variation. To obtain a best least squares fit of observed and modeled variations, the amplitude of the reconnection electric field variation, E_{no}, must be adjusted. Figure 6 shows the E_{no} required to give the best fit to the observed variations of Λ_{OCB} (solid line) and Φ_{PC} (dot-dash line), both as a function of τ_{OCB}. It can be seen that a considerably larger/smaller E_{no} is required (than the 114 mV m^{-1} used in Figures 4 and 5) to fit the observed Λ_{OCB} variation at low/high τ_{OCB}. Conversely, smaller/larger E_{no} is required to fit the observed Φ_{PC} variation at low/high τ_{OCB}. The two curves meet near τ_{OCB} of 10 min. and E_{no} of 110 mV m^{-1}, for which the correlations shown in Figure 5 are both near their peak values.

[23] Figure 7 refines these estimates yet further by plotting the mean square deviation of the N pairs of observed and modeled OCB latitudes ($\Sigma_N\{\Lambda_o - \Lambda_m\}^2/N$), as a function of τ_{OCB}. The E_{no} value used is varied according to the dot-dashed line in Figure 6, i.e., for every τ_{OCB} we

use the E_{no} which gives the best-fit to the observed Φ_{PC} values. The solid line marks the minimum mean-square deviation, Δ_{ms}, which is found at a τ_{OCB} of 9.7 min. The horizontal dot-dash line shows a mean square deviation which we can resolve as significantly larger than this minimum value. We take $\delta\Lambda = 0.5°$ to be the uncertainty of each of the N measurements of Λ_o by FUV and this causes an uncertainty in the mean square value of the latitude difference of $\delta_{ms} = \delta\Lambda(2/N)^{1/2}$. The dot-dash line is at $(\Delta_{ms} + \delta_{ms})$ sets an uncertainty range in τ_{OCB} of 8.4–10.9 min (marked by vertical dot-dash lines). For comparison, the less stringent limits from the correlation analysis (i.e., the vertical dashed lines from Figure 5) are also shown.

[24] If we return to Figure 6, we can use these derived best-estimates and uncertainties in τ_{OCB} to evaluate the corresponding values of the peak electric field, E_{no}. The correlation analysis of modeled and observed transpolar voltage, Φ_{OCB}, gives a best estimate of τ_{OCB} of 10 min, with an uncertainty range of 6–17 min. This gives a best E_{no} estimate of 111 mV m^{-1}, with an uncertainty range of 87–142 mV m^{-1} (the dashed lines in Figure 6). The analysis of the minimum mean-square deviation of modeled
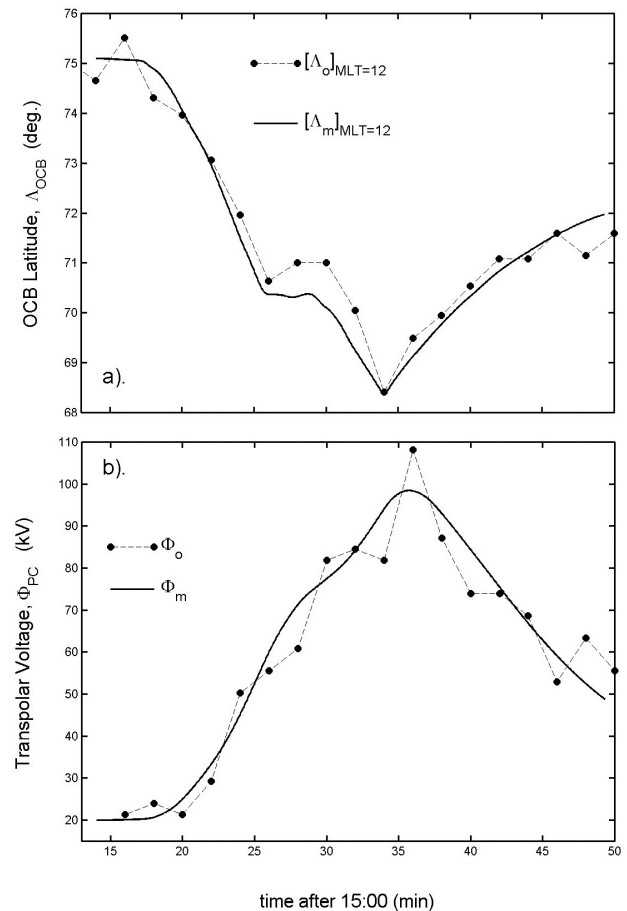
Figure 8. Observed and best-fit model variations, using the same format as Figure 4. (a) Modeled and observed noon-time OCB latitudes, Λ_m and Λ_o. (b) Modeled and observed transpolar voltages Φ_m and Φ_o. The predicted variations are for the best-fit estimates of $\tau_{OCB} = 9.7$ min and $E_{no} = 108$ mV m^{-1}.
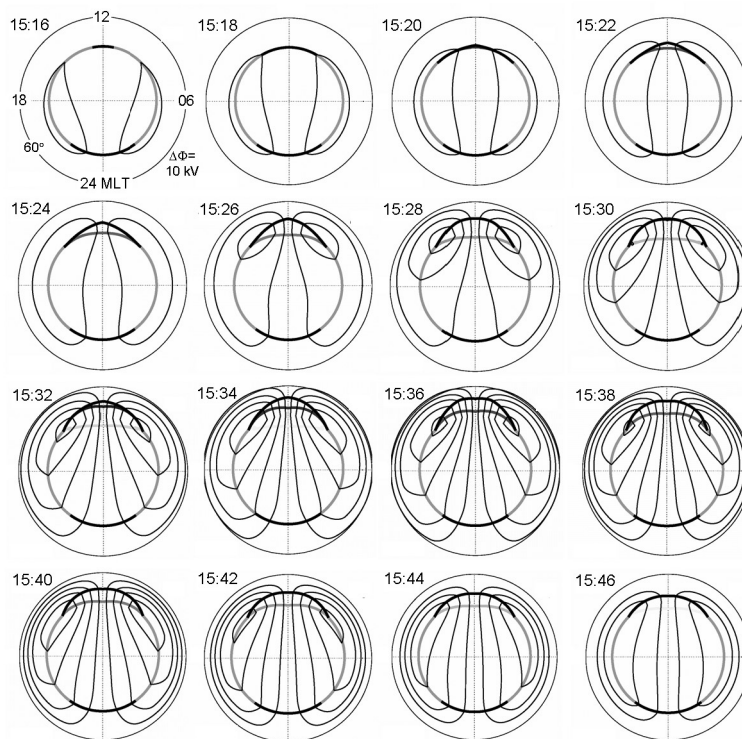
Figure 9. Model convection patterns for the same times as the SuperDARN data shown in Figure 2 of Paper I. The ionospheric projections of the dayside and tail reconnection X-lines are shown as thick black lines and the "adiaroic" (nonreconnecting) open-closed boundary segments by thinner lines. The broadly east-west grey lines poleward of the dayside merging gap show field lines opened at the onset of the two swings of the IMF clock angle, θ, to larger values. Patterns are 2 min apart and are for 1518–1548 UT. The convection patterns are for the optimum estimates for τ_{OCB} and E_{no} of 9.7 min and 108 mV m^{-1}, respectively.

and observed Λ_{OCB} presented above gives $\tau_{OCB} = 9.7 \pm 1.3$ min., which Figure 6 shows corresponds to $E_{no} = 108 \pm 7$ mVm^{-1} (dot-dashed lines).

[25] Figure 8 shows the model predictions of Φ_{PC} and Λ_{OCB} for these best estimates of τ_{OCB} and E_{no} and compares them with the observed values, using the same format as Figure 4. It can be seen that the model reproduces both the observed noontime OCB latitude and the transpolar voltage very well. Thus the model provides quantitative confirmation of the consistency of the erosion and the inductive smoothing of the reconnection voltage, as discussed quantitatively by *Lockwood and Cowley* [1992] and *Cowley and Lockwood* [1992].

[26] Figure 9 shows the convection patterns derived by the model for the observed IMF clock angles (lagged using the best-fit propagation delay variation confirmed in Figure 7 of Paper I). The panels are for the times of the radar scans and are arranged so that they correspond to those in Figure 2 of Paper I. The ionospheric projections of the dayside and tail reconnection X-lines are shown as thick black lines and the "adiaroic" (nonreconnecting) open-closed boundary segments by thick grey lines. The thin black lines are flow streamlines that are 10 kV apart. The grey lines poleward of the dayside merging gap show field lines opened at the onset of the two swings of the IMF clock angle θ to larger values. These lines mark where cusp ion steps would be found and in Figure 9 they fade in successive frames as $\{t_s - t_o\}$

increases and the magnitude of the cusp ion step decreases [*Lockwood*, 1995; *Lockwood and Davis*, 1995, 1996]. The patterns of flow show strong similarities to those observed in Figure 2 of Paper I, allowing for the lack of any IMF B_Y effects and lobe-stirring reconnection.

3.3. Comparison With DMSP Precipitation Observations

[27] We here present a study of a pass of the DMSP-F12 satellite across the southern hemisphere polar cap during the first of the two intensifications of the proton aurora. This is the only available satellite pass which we can contrast to the preevent situation shown in Figure 2. Because the pass is in the southern hemisphere, in Figure 10 we have mirrored both the proton aurora and the flow streamlines observed in the northern hemisphere about the dawn-dusk meridian to allow for dawn-dusk asymmetries associated with the IMF B_Y component. This has the effect of moving the proton emission on newly opened field lines into the dawn sector, consistent with the dawn-dusk asymmetry in the reconnection site predicted by *Cowley et al.* [1991] for the prevailing IMF at this time and over the preceding 6 min (i.e., $B_z < 0$, $B_y > 0$). The flows observed in the dayside polar cap in the northern hemisphere at this time are antisunward and toward dawn and in Figure 10 they therefore appear as antisunward and toward dusk, again consistent with the prevailing IMF orientation [e.g., *Greenwald et al.*, 1990].
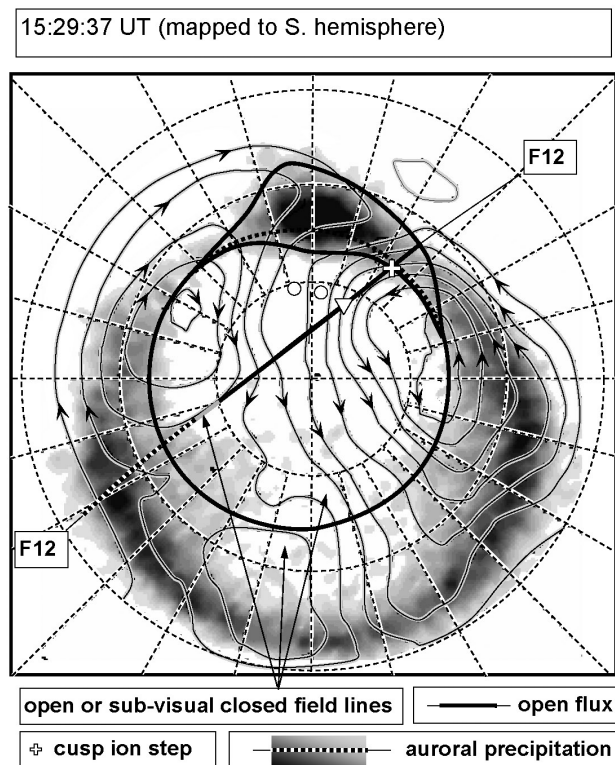
Figure 10. Image of the Doppler-shifted Lyman-α emission recorded by the FUV/SI-12 recorded at 1529:37 UT, with superposed potential streamlines from the 90-s Super-DARN radar scans commencing at 1528:00. The format is the same as in Figure 3; however, the image and flow pattern have been mapped to the southern hemisphere by mirroring both about the noon-midnight meridian to allow for IMF-associated dawn-dusk asymmetries. The pass of DMSP F12, which traversed the southern hemisphere polar cap between 1529:02 and about 1538 UT is also shown. Segments of this pass are marked according to the particle precipitations shown in Figure 11, as in Figure 3. After entering the open field line region at 1529:02, F12 observed dispersed cusp ions with descending energies until 1530:00 (marked on orbit with a cross) when a cusp ion step was observed. At 1532:02 (marked by an inverted triangle), F12 encountered a change in character of the open flux precipitation which is consistent with a remnant signature of the lobe reconnection site, as seen in the earlier northern-hemisphere passes by F12 and F14 when the IMF was northward (mapped to the southern hemisphere at the open circles). The dotted line shows the estimated dayside polar cap boundary from Figure 3 and the solid lines bound the area where the new cusp proton emission exceeds 2 kR. The magnetic flux within this area is 0.8×10^8 Wb.
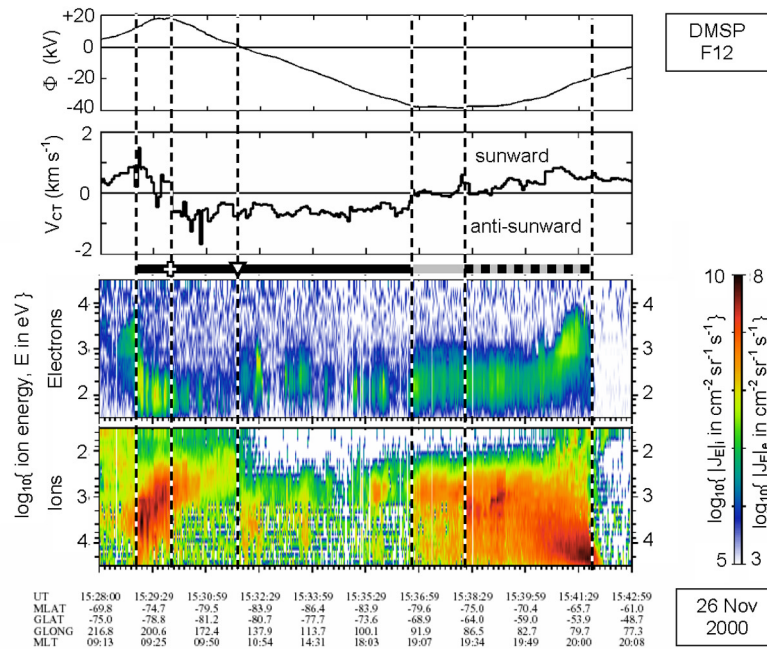
[28] Figure 11 shows the F12 observations during this pass. Between the second and third panels is a shading and symbols key which is also used in Figure 10 and so allows observed features to be placed in the context of the patterns of convective flow and proton aurora. The top two panels show the cross-track convection component and the potential, as used in section 2.1. The lower two panels show the electron and ion precipitation, with the observed electron

and ion differential energy flux ($|J_E|_e$ and $|J_E|_i$ color-coded as a function of energy and time (note that the ion energy scale is inverted). Between 1529:02 and 1530:00 DMSP-F12 observes a typical southward-IMF cusp ion dispersion signature (between the equatorward edge of the dayside open field line region and the point marked with a cross in Figure 10), in which the ion energies fall as the satellite moves poleward across the cusp. However, the ion energies decrease in a downward step discontinuity at 1530:00 (the point marked by the cross). Figure 10 shows that this step maps to the poleward boundary of the enhanced cusp proton aurora and so marks the location of the boundary between newly opened field lines produced by the burst of southward IMF and older open field lines produced by earlier periods of southward IMF. The location of this step is marked in the model predictions by the grey line in the corresponding panel of Figure 9. Thus this is a clear example of a temporal cusp ion step [*Lockwood and Davis*, 1996], generated by pulsed reconnection, and in this case the reconnection pulse is driven by the upstream IMF clock angle (see discussion of temporal and spatial cusp ion steps by *Lockwood* [1995, 1996]). Cusp precipitation is observed until 1531:54 (marked with a triangle), after which structured ion and electron precipitation was observed. The open circles in Figure 10 are the lobe reconnection sites that were seen before the southward turning of the IMF (also shown in Figure 3) and the structured precipitation to the nightside of these locations was typical of the polar cap before the IMF turned southward.

[29] Figure 10 shows that the cusp ion step is seen in the expected location, as is the dayside OCB, relative to the enhanced Lyman-α emission. Both these features seen by DMSP-F12 fall close to the 2 kR intensity contour and using this threshold gives the boundaries to the region of newly opened flux shown by the solid lines in Figure 10. It can be seen that the inferred and observed (from FUV/SI-12 and DMSP-F12, respectively) OCB has eroded equatorward and that the inferred and observed poleward edge of the newly opened flux has convected antisunward, as predicted in Figure 9. The newly opened flux encompassed by these lines in Figure 10 equals 0.8×10^8 Wb, which matches well the polar cap flux increase predicted by the model for this time ($\Delta F_{PC} = 0.75 \times 10^8$ Wb, see Figure 2). Thus the rate of growth of the region of newly opened flux inferred from FUV/SI-12 as well as the OCB and cusp ion step locations observed by DMSP-F12, provide further support for the convection and aurora modeling presented in this paper and in Paper I and the time constants on which it is based.

[30] Immediately equatorward of the step the ion energy had fallen to 33 eV, which for a typical field-aligned distance to a low-latitude magnetopause reconnection site of 20 R_E yields a proton flight time of 9 min, indicating the first field lines in the pulse to be opened were reconnected at about 1521. This is just after the first signatures of the onset of reconnection in the SuperDARN and FUV data at about 1519, but this delay is consistent with the 2.5 min required for the reconnection to spread azimuthally from noon to the observation site near 9.5 MLT, as used as an input to the model ($d\phi_r/dt$ in input I.3). Thus the data are consistent with all the field lines in the dispersed cusp ion feature observed by F12 between 1529:02 and 1530:00 being produced by the first reconnection pulse.

Figure 11. Observations by the DMSP F12 spacecraft during the pass through the southern polar cap. The top panel shows the along-track distribution of potential, Φ, derived from the cross-track plasma velocity, V_{CT}, shown in the second panel. The third and fourth panels show energy-time spectrograms of the differential energy flux of, respectively, electrons and ions ($|J_E|_e$ and $|J_E|_i$), color-contoured as a function of energy E and time. Note that in the bottom panel the ion energy axis has been inverted. Vertical dashed lines give key times and locations, and the bar code between panels 2 and 3 of the present figure is also used in Figure 10.

[31] Note that the flow seen by F12 (and in the mirrored SuperDARN data from the opposite hemisphere) in the region of newly opened flux remains sunward where the cusp ion dispersion typical of southward IMF (with ion energies falling with increasing latitude) is observed. This proves that the dispersed cusp is not caused by poleward convection in this case (as it would be in a steady-state case) but by the equatorward erosion of the OCB caused by the reconnection pulse. Note also that the convection reversal boundary, as seen by F12 and SuperDARN, and hence the region 1 currents, are at the poleward edge of the region of newly opened flux and hence are poleward of the OCB and thus on open field lines. Again this situation is not predicted for the steady-state case but is a natural consequence of the rapid boundary erosion in the time-dependent case.

4. Discussion and Conclusions

[32] We have used the combination of global imaging of the ionospheric convection pattern and of the proton aurora (by the SuperDARN radar network and the FUV/SI-12 instrument of the IMAGE satellite, respectively) to demonstrate quantitatively the concepts of ionospheric flow excitation proposed by *Cowley and Lockwood* [1992]. Specifically, the equatorward erosion near noon has been shown to be consistent, in both amplitude and waveform, with the "inductive smoothing" of the transpolar voltage predicted by the theory. From the best fits of the modeled variation we estimate the relaxation time constant of the OCB to be $\tau_{OCB} = 9.7 \pm 1.3$ min (which gives a peak

OCB-tangential electric field, E_{no} of 108 ± 7 mV m^{-1} in this case).

[33] This estimate of the time constant is consistent with, but slightly shorter than, the ~15 min deduced from the first observations of the flow response to IMF changes [*Etemadi et al.*, 1988; *Todd et al.*, 1988] and slightly longer than more recent reported estimates of ≈ 8 min [e.g., *Khan and Cowley*, 1999; *Murr and Hughes*, 2001]. The value is also consistent with that derived by *Sanchez et al.* [1991] using and inductive circuit analogy.

[34] The time constant is "inductive" as it involves the growth and decay of magnetic flux threading the magnetopause to ionosphere current loop [*Lockwood and Cowley*, 1992; LM04]. Circuit analogies must be used with care in the magnetosphere because field-aligned currents can move and are not constrained to wires as they are in laboratory circuits. Nevertheless, the current in this loop must flow through the ionosphere, providing the electrical resistance R, which in the analogy gives the time constant $\tau = LR$, where L is the inductance of the analogous circuit [*Sanchez et al.*, 1991]. Thus this analogy predicts that the time constant τ_{OCB} will, in general, depend on the ionospheric conductivity (and hence on MLT, season, and the local precipitation characteristics) and the balance of stresses in the magnetosphere which allow field reconfiguration and so determine the inductance.

[35] Initial additional investigations (not presented here) show that generalizing τ_{OCB} to be a function of MLT had negligible effect on the analysis reported in the present paper for the noon OCB but did have an effect on the

amplitude and delay of OCB movement predicted nearer dawn and dusk. However, in the observations presented here, any such effects are masked by those of the polarity switch in IMF B_y which preferentially adds newly opened flux to either the dawn or dusk flank and so shifts the polar cap center [*Cowley et al.*, 1991]. In addition, defining the OCB from the poleward edge of detected precipitation on closed field lines is often misleading away from noon. Thus the value of $\tau_{OCB} = 9.7 \pm 1.3$ min derived here applies to noon and may not apply elsewhere. However, we should not expect this noontime value to always apply. For example, in summer the higher conductivities would, according to the LR circuit analogy, tend to give a lower time constant on the dayside. There may also be effects on the effective dayside inductance associated with the dipole tilt. We therefore would wish to repeat the analysis presented here to any similar events at other times of year to search for any such dependencies.

[36] The maps of ionospheric convection generated in the model simulations, using the best fit τ_{OCB} and E_{no}, are similar in their general form to those observed (compare Figure 9 with Figure 2 of Paper I). However, various features cannot be reproduced by the model in its present form. Specifically, the LM04 model deals with the transfer of magnetic flux into and out of the open field line polar cap by low-latitude reconnection and it does not include effects taking place within the polar cap. Thus the east-west flows on newly opened field lines, caused by the Svalgaard-Mansurov effect and associated with the Y-component of the IMF, are not included nor is any stirring of polar cap caused by high-latitude (lobe) reconnection in one hemisphere. Note, however, that any field line closure by lobe reconnection in both hemispheres can be included as a reverse-polarity tangential electric field along the dayside OCB.

[37] The maps of cusp proton aurora intensity, produced using the flows predicted by the model for the best-fit τ_{OCB} and E_{no}, along with the cusp ion precipitation and proton aurora model discussed in Paper 1, are shown in Figure 9 of Paper I. It can be seen that the predicted deformation of the dayside OCB is very similar to that inferred from the FUV/SI-12 observations (see Figure 2 of Paper I). Thus the model is reproducing the behavior of the dayside flows and OCB rather well. This is the first time that the LM04 model has been applied to observations and indicates that the clock angle dependence of the reconnection rate employed, namely $\sin^4(\theta/2)$, is adequate. Further studies will compare the results presented here with the results for other functions of IMF θ and B_Z and evaluate their performance of various proposed coupling functions.

[38] In predicting the evolution of the OCB latitude and the transpolar voltage, the model also correctly predicts the appearance of a cusp ion step in the DMSP precipitation data. The equatorward erosion of the boundary explains why the dispersion equatorward of this step is typical of antisunward flow yet lies on sunward flowing field lines. The model also explains other anomalous features, such as the cusp precipitation being present equatorward of the region 1 currents and the convection reversal boundary.

References

Ahn, B.-H., Y. Kamide, H. W. Kroehl, and D. J. Gorney (1992), Cross-polar potential difference, auroral electrojet indices, and solar wind parameters, *J. Geophys. Res.*, 97, 1345–1352.

Akasofu, S. I. (1981), Energy coupling between the solar wind and the magnetosphere, *Space Sci. Rev.*, 28, 121–190.

Banks, P. M., T. Araki, C. R. Clauer, J. P. St-Maurice, and J. C. Foster (1984), The interplanetary magnetic field, cleft currents, and plasma convection in the polar caps, *Planet. Space Sci.*, 32, 1551–1560.

Burch, J. L. (1973), Rate of erosion of dayside magnetic flux based on a quantitative study of polar cusp latitude on the interplanetary magnetic field, *Radio Sci.*, 8, 955–961.

Clauer, C. R., and P. M. Banks (1986), Relationship of interplanetary electric field to the high latitude ionospheric electric field and currents: Observations and model simulation, *J. Geophys. Res.*, 91, 6959–6971.

Cowley, S. W. H., and M. Lockwood (1992), Excitation and decay of solar-wind driven flows in the magnetosphere-ionosphere system, *Ann. Geophys.*, 10, 103–115.

Cowley, S. W. H., J. P. Morelli, and M. Lockwood (1991), Dependence of convective flows and particle precipitation in the high-latitude dayside ionosphere on the X and Y components of the interplanetary magnetic field, *J. Geophys. Res.*, 96, 5557–5564.

Eather, R. H. (1985), Polar cusp dynamics, *J. Geophys. Res.*, 90, 1569–1576.

Elphinstone, R. D., D. J. Hearn, J. S. Murphree, and L. L. Cogger (1991), Mapping using the Tsyganenko long magnetospheric model and its relationship to Viking auroral images, *J. Geophys. Res.*, 96, 1467–1480.

Elphinstone, R. D., J. S. Murphree, D. J. Hearn, L. L. Cogger, P. T. Newell, and H. Vo (1992), Viking observations of the UV dayside aurora and their relationship to DMSP particle boundary definitions, *Ann. Geophys.*, 10, 815–826.

Etemadi, A., S. W. H. Cowley, M. Lockwood, B. J. I. Bromage, D. M. Willis, and H. Lühr (1988), The dependence of high-latitude dayside ionospheric flows on the north-south component of the IMF: A high time resolution correlation analysis using EISCAT "POLAR" and AMPTE UKS and IRM data, *Planet. Space Sci.*, 36, 471–498.

Fedder, J. A., C. M. Mobarry, and J. G. Lyon (1991), Reconnection voltage as a function of IMF clock angle, *Geophys. Res. Lett.*, 18, 1047–1050.

Freeman, M. P. (2003), A unified model of the response of ionospheric convection to changes in the interplanetary magnetic field, *J. Geophys. Res.*, 108(A1), 1024, doi:10.1029/2002JA009385.

Freeman, M. P., and D. J. Southwood (1988), The effects of magnetospheric erosion on mid- and high- latitude ionospheric flows, *Planet. Space Sci.*, 36, 509–522.

Greenwald, R. A., K. B. Baker, J. M. Ruohoniemi, J. R. Dudeney, N. Pinnock, N. Mattin, J. M. Leonard, and R. P. Lepping (1990), Simultaneous conjugate observations of dynamic variations in high-latitude dayside convection due to changes in IMF B_y, *J. Geophys. Res.*, 95, 8057–8072.

Horwitz, J. L., and S.-I. Akasofu (1977), The response of the dayside aurora to sharp northward and southward transitions of the interplanetary magnetic field and to magnetospheric substorms, *J. Geophys. Res.*, 82, 2723–2734.

Khan, H., and S. W. H. Cowley (1999), Observations of the response time of high-latitude ionospheric convection to variations in the interplanetary field using EISCAT and IMP-8 data, *Ann. Geophys.*, 17, 1306–1355.

Knipp, D. J., A. D. Richmond, B. Emery, N. U. Crooker, O. de la Beaujardiere, D. Evans, and H. Kroehl (1991), Ionospheric convection response to changing IMF direction, *Geophys. Res. Lett.*, 18, 721–724.

Knipp, D. J., et al. (1993), Ionospheric convection response to strong, slow variations in a northward interplanetary magnetic field: A case study for January 14, 1988, *J. Geophys. Res.*, 98, 19,273–19,292.

Leontyev, S. V., G. V. Starkov, V. G. Vorobjev, and V. L. Zverev (1992), Dayside aurorae and their relations to other geophysical phenomena, *Planet. Space Sci.*, *40*, 621–639.

Lockwood, M. (1995), Ground-based and satellite observations of the cusp: Evidence for pulsed magnetopause reconnection, in *Physics of the Magnetopause*, *Geophys. Monogr. Ser.*, vol. 90, edited by P. Song, B. U. O. Sonnerup, and M. F. Thomsen, pp. 417–426, AGU, Washington, D. C.

Lockwood, M. (1996), The case for transient magnetopause reconnection, *Eos Trans. AGU*, *77*(26), 246–250.

Lockwood, M. (2002), An evaluation of the correlation between open solar flux and total solar irradiance, *Astron. Astrophys.*, *382*, 678–687.

Lockwood, M., and S. W. H. Cowley (1992), Ionospheric convection and the substorm cycle, in *Substorms 1, Proceedings of the First International Conference on Substorms, ICS-1, ESA-SP-335*, edited by C. Mattock, pp. 99–109, Eur. Space Agency Publ., Nordvijk, Netherlands.

Lockwood, M., and C. J. Davis (1995), The occurrence probability, width and number of steps of cusp precipitation for fully pulsed reconnection at the dayside magnetopause, *J. Geophys. Res.*, *100*, 7627–7640.

Lockwood, M., and C. J. Davis (1996), On the longitudinal extent of magnetopause reconnection bursts, *Ann. Geophys.*, *14*, 865–878.

Lockwood, M., and S. K. Morley (2004), A numerical model of the ionospheric signatures of time-varying magnetic reconnection: I. Ionospheric convection, *Ann. Geophys.*, *22*, 73–91.

Lockwood, M., J. Moen, S. W. H. Cowley, A. D. Farmer, U. P. Løvhaug, H. Lühr, and V. N. Davda (1993), Variability of dayside convection and motions of the cusp/cleft aurora, *Geophys. Res. Lett.*, *20*, 1011–1014.

Lockwood, M., B. S. Lanchester, H. U. Frey, K. Throp, S. K. Morley, S. E. Milan, and M. Lester (2003), IMF control of cusp proton emission intensity and dayside convection: Implications for component and antiparallel reconnection, *Ann. Geophys.*, *21*, 955–982.

Lockwood, M., J. Moen, A. P. van Eyken, J. A. Davies, K. Oksavik, and I. W. McCrea (2005), Motion of the dayside polar cap boundary during substorm cycles: I. Observations of pulses in the magnetopause reconnection rate, *Ann. Geophys.*, *23*, 3495–3511.

Lu, G., P. H. Reiff, M. R. Hairston, R. A. Heelis, and J. L. Karty (1989), Distribution of convection potential around the polar cap boundary as a function of interplanetary magnetic field, *J. Geophys. Res.*, *94*, 13,447–13,461.

Lu, G., S. W. H. Cowley, S. E. Milan, D. G. Sibeck, R. A. Greenwald, and T. Moretto (2002), Solar wind effects on ionospheric convection: A review, *J. Atmos. Sol. Terr. Phys.*, *64*, 145–157.

McCrea, I. W., M. Lockwood, J. Moen, F. Pitout, P. Eglitis, A. D. Aylward, J.-C. Cerisier, A. Thorolfsson, and S. E. Milan (2000), ESR and EISCAT observations of the response of the cusp and cleft to IMF orientation changes, *Ann. Geophys.*, *18*, 1009–1026.

Mende, S. B., H. Heetderks, and H. U. Frey (2000a), Far ultraviolet imaging from the IMAGE spacecraft, 1. System design, *Space Sci. Rev.*, *91*, 243–270.

Mende, S. B., H. Heetderks, and H. U. Frey (2000b), Far ultraviolet imaging from the IMAGE spacecraft, 3. Spectral imaging of Lyman alpha and OI 135.6 ηm, *Space Sci. Rev.*, *91*, 287–318.

Milan, S. E., M. Lester, S. W. H. Cowley, K. Oksavik, M. Brittnacher, R. A. Greenwald, G. Sofko, and J.-P. Villain (2003), Variations in polar cap area during two substorm cycles, *Ann. Geophys.*, *21*, 1121–1140.

Moen, J., M. Lockwood, K. Oksavik, H. C. Carlson, W. F. Denig, A. P. van Eyken, and I. W. McCrea (2004), The dynamics and relationships of precipitation, temperature and convection boundaries in the dayside auroral oval, *Ann. Geophys.*, *22*, 4381–4395.

Murr, D. L., and W. J. Hughes (2001), Reconfiguration timescales of ionospheric convection, *Geophys. Res. Lett.*, *28*, 2145–2148.

Newell, P. T., and C.-I. Meng (1992), Mapping the dayside ionosphere to the magnetosphere according to particle precipitation characteristics, *Geophys. Res. Lett.*, *19*, 609–612.

Reiff, P. H., R. W. Spiro, and T. W. Hill (1981), Dependence of polar cap potential drop on interplanetary parameters, *J. Geophys. Res.*, *86*, 7639–7648.

Ridley, A. J., C. R. Clauer, G. Lu, and V. O. Papitashvilli (1997), Ionospheric convection during nonsteady interplanetary magnetic field conditions, *J. Geophys. Res.*, *102*, 14,563–14,573.

Ridley, A. J., G. Lu, C. R. Clauer, and V. O. Papitashvilli (1998), A statistical study of the ionospheric convection response to changing interplanetary magnetic field conditions using the assimilative mapping of ionospheric electrodynamics technique, *J. Geophys. Res.*, *103*, 4023–4039.

Ruohoniemi, J. M., and K. B. Baker (1998), Large-scale imaging of high-latitude convection with Super Dual Auroral Radar Network HF radar observations, *J. Geophys. Res.*, *103*, 20,797–20,812.

Ruohoniemi, J. M., and R. A. Greenwald (1998), The response of high latitude convection to a sudden southward IMF turning, *Geophys. Res. Lett.*, *25*, 2913–2916.

Ruohoniemi, J. M., S. G. Shepherd, and R. A. Greenwald (2002), The response of the high-latitude ionosphere to IMF variations, *J. Atmos. Sol. Terr. Phys.*, *64*, 159–171.

Samson, J. C., D. D. Wallis, T. J. Hughes, F. Creutzberg, J. M. Ruohoniemi, and R. A. Greenwald (1992), Substorm intensifications and field line resonances in the nightside magnetosphere, *J. Geophys. Res.*, *97*, 8495–8518.

Sanchez, E. R., G. L. Siscoe, and C.-I. Meng (1991), Inductive attenuation of the transpolar voltage, *Geophys. Res. Lett.*, *18*, 1173–1176.

Sandholt, P. E. (1988), IMF control of the polar cusp and cleft auroras, *Adv. Space Res.*, *8*, (9)21–(9)34.

Sandholt, P. E., A. Egeland, J. A. Holtet, B. Lybekk, K. Svenes, and S. Asheim (1985), Large- and small-scale dynamics of the polar cusp, *J. Geophys. Res.*, *90*, 4407–4414.

Stubbs, T. J., M. Lockwood, P. Cargill, J. Fennel, M. Grande, B. Kellett, C. H. Perry, and A. Rees (2001), Dawn/dusk asymmetry in particles of solar wind origin within the magnetosphere, *Ann. Geophys.*, *19*, 1–9.

Throp, K., M. Lockwood, B. S. Lanchester, S. K. Morley, and H. U. Frey (2005), Modeling the observed proton aurora and ionospheric convection responses to changes in the IMF clock angle: 1. Persistence of cusp proton aurora, *J. Geophys. Res.*, *110*, A12311, doi:10.1029/2003JA010306.

Todd, H., S. W. H. Cowley, M. Lockwood, D. M. Willis, and H. Lühr (1988), Response time of the high-latitude dayside ionosphere to sudden changes in the north-south component of the IMF, *Planet. Space Sci.*, *36*, 1415–1428.

Vasyliunas, V. M., J. R. Kan, G. L. Siscoe, and S.-I. Akasofu (1982), Scaling relations governing magnetospheric energy transfer, *Planet Space Sci.*, *30*, 359–365.

Vorobjev, V. G., G. Gustafsson, G. V. Starkov, Y.-I. Feldstein, and N. F. Shevnina (1975), Dynamics of day and night aurora during substorms, *Planet Space Sci.*, *23*, 269–278.

Wygant, J. R., R. B. Torbert, and F. S. Mozer (1983), Comparison of S3-2 polar cap potential drops with the interplanetary magnetic field and models of magnetopause reconnection, *J. Geophys. Res.*, *88*, 5727–5735.

————————————

H. U. Frey, Space Sciences Laboratory, University of California, Berkeley, Berkeley, CA 94720-7450, USA.

B. S. Lanchester, M. Lockwood, and K. Throp, Department of Physics and Astronomy, Southampton University, Highfield, Southampton, Hampshire SO9 5NH, UK. (m.lockwood@rl.ac.uk)

M. Lester and S. E. Milan, Department of Physics and Astronomy, Leicester University, University Road, Leicester LE1 7RH, UK.

S. K. Morley, CRC for Satellite Systems, School of Mathematical and Physical Sciences, University of Newcastle, Callaghan, New South Wales, NSW 2308, Australia.